

## Effect of Sintering Method on Corrosion Resistance of Ti-40Nb-15Zr Alloy for Biomedical Applications in Simulated Body Fluid

Jianming Ruan<sup>1\*</sup>, Taomei Zhang<sup>1</sup>, Baoqi Wang<sup>1</sup>, Hailin Yang<sup>1</sup> and Wei Ruan<sup>2</sup>

<sup>1</sup>State Key Laboratory of Powder Metallurgy, Central South University, Changsha 410083, China

<sup>2</sup>Department of Anesthesiology, The Second Xiang Ya Hospital, Central South University, Changsha 410011, PR China

\*Corresponding author: Jianming Ruan, 1State Key Laboratory of Powder Metallurgy, Central South University, Changsha 410083, China, Tel: 15802501179; E-Mail: jianming@csu.edu.cn

Received: August 06, 2018; Accepted: August 13, 2018; Published: August 21, 2018

### Abstract

Ti-40at.%Nb-15at.%Zr (TNZ) alloy was prepared by high vacuum sintering (HVS) and spark plasma sintering (SPS) using Zr, Nb, and Ti elemental powder. X-ray diffraction (XRD) and Scanning electron microscopy (SEM) and electrochemical measurement were used to character the corrosion resistance of the alloys in Hank's solution. The results indicated that HVSe alloy was consisted of  $\alpha$  and  $\beta$ , and the SPSe alloy was characterized by rich-Nb phase and less porosity. Additionally, the SPSe alloy has the lower corrosion current ( $I_{\text{corr}}$ ) value 0.026  $\mu\text{A}/\text{cm}^2$  than Ti-6Al-4V and HVSe alloy which were 0.043  $\mu\text{A}/\text{cm}^2$  and 0.032  $\mu\text{A}/\text{cm}^2$ , respectively. The SEM results of the samples after immersion in the Hank's solution for 72 hours showed that the corrosion of the SPSe alloy started in the rich-Nb region, and that of the HVSe alloy firstly occurred at the interface of the two phases ( $\alpha$  and  $\beta$ ). Furthermore, the EIS results demonstrated the existence of a duplex film consisting of an inner barrier layer and a porous outer layer on both Ti-6Al-4V and SPSe alloys.

**Keywords:** Ti-Nb-Zr; Powder metallurgy; EIS; Passive film; Hank's solution

### Introduction

Development of implant biomaterials has attracted wide attention in recent years. Titanium alloys have been widely used for implant application thanks to its favorable mechanical properties, remarkable biocompatibility and corrosion resistance [1,2]. Ti-6Al-4V (T64) alloy was a typical titanium alloy used for biomaterials [3,4]. However, "stress shielding" always occurred due to the elastic mismatch between Ti64, which has an elastic modulus of -110 GPa, and the surrounding human bones, whose elastic modulus ranges from 10-30 GPa [5,6]. This kind of stiffness mismatch can lead to serious issues, such as bone resorption and implant loosening [7]. Moreover, the diffusion of these alloying elements such as Al and V are likely to bring forth allergic reactions and impact the cell viability, finally triggering serious health problems. In order to develop new types of titanium alloys, some scholars came up with near  $\beta$  type titanium alloys with Nb and Ta, non-toxic and non-allergic

**Citation:** Ruan J, Zhang T, Wang B, et al. Effect of Sintering Method on Corrosion Resistance of Ti-40Nb-15Zr Alloy for Biomedical Applications in Simulated Body Fluid. Anal Chem Ind J. 2018;18(2):137

© 2018 Trade Science Inc.

alloying elements, which have the potential of lowering the elastic modulus [8-11]. It also has been found that Zirconium has good biocompatibility and corrosion resistance, and has been confirmed to be harmless to the human body [12]. Simultaneously, Zr can effectively enhance the mechanical properties of titanium-based alloys [13,14]. However, according to a lot of reports, most of the biological materials are prepared by casting, and few by powder metallurgy. Therefore, less research was carried out about the effect of sintering method on corrosion performance of alloys.

Spark plasma sintering (SPS), a new-type activated sintering technology, can effectively promote the sintering densification process and inhibit the grain growth. It is worth pointing out that the mixing uniformity of raw materials in powder metallurgy often cannot reach the atomic level. The short holding time of SPS increases the chance of element enrichment in comparison with the traditional vacuum sintering technology.

In this study, the Ti-40Nb-15Zr alloy was prepared by traditional high vacuum sintering (HVS) technology and spark plasma sintering (SPS), respectively. The aim is to explore the influence of sintering method on the corrosion behavior of Ti-40Nb-15Zr alloy in a simulated body fluid and improve the sintering method for stronger corrosion resistance of the alloy. It has been reported that the body fluid environment is equivalent to a complex electrolytic pool in which implant materials are susceptible to electrolytic corrosion. The electrochemical corrosion behavior and corrosion mechanism of the alloys in Hank's solution were investigated by measuring the open circuit potential (OCP), potentiodynamic polarization curves and electrochemical impedance spectroscopy (EIS).

## **Materials and methods**

### **Materials preparation**

Elemental powder of Zr (99.9%), Nb (99.9%), and Ti (99.9%) have been blended for 5 h at 300 rpm with a nominal composition of Ti-40Nb-15Zr (at.%). Two types of sintering, traditional high vacuum sintering (HVS) and spark plasma sintering (SPS), were used to prepare the samples. Prior to high vacuum sintering (HVS), the elemental powders were mixed and compacted under a hydraulic press at 200 MPa to form a green compact, then the sintering of the green compacts was conducted in a vacuum furnace under high vacuum ( $<10^{-3}$  Pa), at a sintering temperature of 1400°C for 2 hours. And the spark plasma sintering (SPS) process involved the sintering of the mixed powders under high vacuum ( $<10^{-3}$  Pa) up to a temperature of 1400°C at a rate of 50°C/min, with a holding time of 10 min, and an axial pressure of 30MPa, followed by rapid cooling.

### **Materials characterization**

The microstructure was examined by scanning electron microscope (Quanta FEG 250) equipped with EDX. The phase structure was identified by an X-ray diffractometer (XRD, D/MAX-2250, Japan) with Cu K $\alpha$  radiation ( $\lambda=1.5418$  Å). The composition of the passivation film on the surface of alloys was detected by X-ray photoelectron spectroscopy (XPS, K-

Alpha, US), which was carried out in a vacuum chamber with micro-concentration monochromatic Al  $K_{\alpha}$  X-ray source. The relative density ( $d$ ) is the fraction of apparent density ( $\rho$ ) to the nominal theoretical density ( $\rho_0$ ) and is determined by Eq. (1)

$$d = \frac{\rho}{\rho_0} \times 100\% \quad (1)$$

$\rho$  can be determined by drainage method according to the principle of Archimedes. The samples with a dimension of 10mm×10mm×5 mm were wire-electrode cut from the sintered samples and ground, polished and ultrasonically cleaned.

### Corrosion characterization

Measurements of all specimens were taken in Hank's solution composed of 8.0g/L NaCl, 0.4 g/L KCl, 0.6 g/L  $\text{KH}_2\text{PO}_4$ , 0.14 g/L  $\text{CaCl}_2$ , 0.1 g/L  $\text{MgCl}_2 \cdot 6\text{H}_2\text{O}$ , 0.35 g/L  $\text{NaHCO}_3$ , 0.06 g/L  $\text{NaH}_2\text{PO}_4 \cdot 2\text{H}_2\text{O}$ , 0.06 g/L  $\text{MgSO}_4 \cdot 7\text{H}_2\text{O}$  and 1 g/L D-Glucose, while maintaining the PH value at 7.4 and testing solution temperature at  $37 \pm 0.5^\circ\text{C}$ . The electrochemical test was conducted on a CHI760E Electrochemical Workstation. The electrochemical system utilizes a standard three-electrode system by using samples as the working electrode, the saturated calomel electrode (SCE) as the reference electrode, and metal platinum with a size of 10mm x 10mm x 1mm as the auxiliary electrode.

Open circuit potential was firstly tested for 600s, and then the electrochemical impedance spectroscopy was tested with respect to the corrosion potential after 2 hours immersion in Hank's solution.

The sine wave signal functioned as an excitation signal with an amplitude of 10 mV and a frequency range of 10-2-105Hz. ZSimpWin 3.0 software was used for analyzing the impedance data. Finally, the measurement of potentiodynamic polarization curves were obtained with a scanning range of -1~2.1 V and a scanning speed of 0.5 mV/s.

## Results and Discussion

### Microstructure and phase composition

The XRD spectra of the Ti-6Al-4V alloy and the Ti-Nb-Zr alloy obtained from different sintering methods were presented in **FIG.1**. It is obvious that the Ti-6Al-4V alloy is mainly composed of  $\alpha$  and  $\beta$  phase. It also shows that the major diffraction peak of HVSed alloy originated from the bcc  $\beta$  phase and the minor peak from the hexagonal  $\alpha$  phase. This is mainly due to the precipitation of supersaturated solid solution during the cooling process. Meanwhile, the diffraction peaks of SPSed alloy originating from the  $\beta$ -Nb phase and  $\beta$ -Ti phase, was owed to inhomogeneous diffusion as a result of the short holding time and rapid cooling rate.

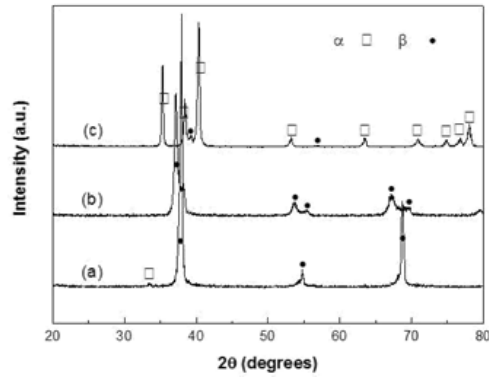


FIG.1. X-ray diffraction patterns of (a) HVSed TNZ, (b) SPSed TNZ and (c)Ti-6Al-4V alloy.

FIG.2 showed the SEM images of the Ti-6Al-4V alloy and the Ti-Nb-Zr alloys. After similar erosion times in a solution composed of 20vol% HNO<sub>3</sub>, 5 vol% HF, and 75 vol% H<sub>2</sub>O, the grain boundary of the HVSed Ti-Nb-Zr alloy was observed clearly and had an average grain size of 52μm. Contrary to the HVSed alloy, the SPSed alloy results exhibited a less obvious grain boundary. As shown in FIG.2(a), there were a few needle-like α phases distributed in the β matrix. And for the SPSed alloy, it was obvious that a rich-Nb phase was distributed in the matrix phase, as shown in FIG.2(b). The presence of α and β phase in the Ti-6Al-4V alloy was similar to the results mentioned in the XRD.

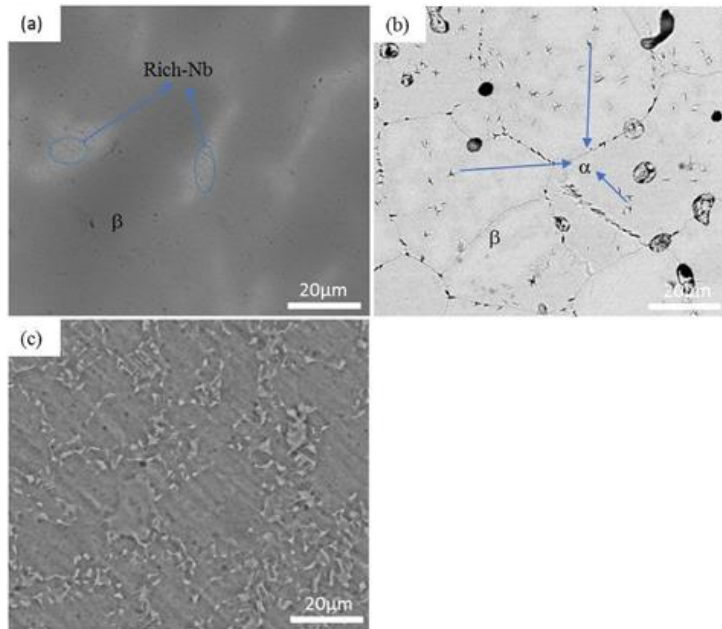
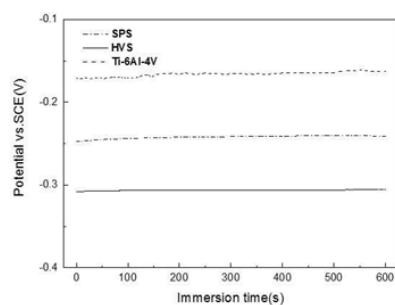


FIG.2. SEM micrographs showing the microstructures of (a) SPSed, (b) HVSed and (c) Ti-6Al-4V.

### Electrochemical corrosion behavior and mechanism

**FIG.3** showed the open circuit potential of Ti-Nb-Zr alloys with different times in Hank's solution, and shows a similar change trend in Ti-6Al-4V alloy, HVSeD and SPSeD alloy with an increase in the initial value before gradually becoming stable, which accords with the theory of electricity neutrality and indicates the formation of a relatively complete passive film on the surface of the Ti alloy in a corrosive environment [15]. According to the test results, open circuit potential of the Ti-6Al-4V alloy is about -0.172V (vs.SCE), which is higher than both the SPSeD and HVSeD alloy, -0.247V and -0.308V (vs.SCE) respectively. The open circuit potential is the electrode potential of the electrode to be tested, which was measured when there is no current flowing through the circuit, that is, the battery is in an open state, and its value indicates the ability to perform an electrochemical reaction for the electrode. Thus indicating that the HVSeD alloy is more prone to electrochemical reactions, in comparison to both the Ti-6Al-4V alloy and the SPSeD alloy. Additionally, Marino et al. [16] have shown that the titanium and titanium alloy can spontaneously form an oxide film composed of TiO, Ti<sub>2</sub>O<sub>3</sub> and TiO<sub>2</sub>. Once contacted with the electrolyte, the TiO and Ti<sub>2</sub>O<sub>3</sub> are transformed into TiO<sub>2</sub>, making the oxide film more stable, which is why the open circuit potential of the three alloys have an upward trend at the beginning of the test.



**FIG.3. Open-circuit potential (OCP) as a function of time for SPSeD, HVSeD and Ti-6Al-4V alloys in the Hank's solution at 37°C.**

**FIG.4** showed the potentiodynamic polarization curves of the Ti-6Al-4V alloy and two kinds of as-sintered alloys in Hank's solution, and the corresponding potentiodynamic polarization curve parameters were listed in **TABLE 1**. It is obvious that these three types of alloys presented apparent activation-passivation reaction in Hank's solution. For corrosive metal electrodes in corrosive media, the stable potential is called the corrosion potential when the circuit is open and the corrosion potential ( $E_{corr}$ ) of SPSeD, HVSeD alloy and the Ti-6Al-4V alloy is -0.062V, -0.552V and -0.023V (vs.SCE), respectively. At this time, the reaction rates of the anode and the cathode are equal, and the corresponding corrosion current represents the rate of progress of the anode dissolution reaction of the metal in the open state and the rate of the cathode reduction reaction in the etching process. The results show that the Ti-6Al-4V has the higher corrosion current ( $I_{corr}$ ) value  $0.043\mu\text{A}/\text{cm}^2$  than SPSeD and HVSeD alloy which are  $0.026\mu\text{A}/\text{cm}^2$  and  $0.032\mu\text{A}/\text{cm}^2$ , respectively. It can be known from the polarization curves that in the initial stage, the anode dissolution current increases as the electrode potential moves forward, which is an active dissolution process, and at which time the anode surface is in an activated state. When the dissolution rate of the metal is almost irrelevant to the change in potential, the surface of the metal material is in a passive state. The Ti-6Al-4V alloy,

SPSed, and HVSed alloy began to produce stable passivation behavior at 0.352V, 0.318V and 0.859V (vs.SCE), correspondingly, the passivation current density of them is  $11.22\mu\text{A}/\text{cm}^2$ ,  $0.618\mu\text{A}/\text{cm}^2$  and  $7.150\mu\text{A}/\text{cm}^2$ , respectively. After entering passivation, the potential of the alloys continues to increase without interruption, indicating that a relatively stable passivation film was formed on the surface of the alloy. Since the charge transfer in the electrode reaction is achieved by the migration of metal ions, covering the metal surface with an oxide film with poor ionic conductivity, limited the dissolution reaction at the metal anode.

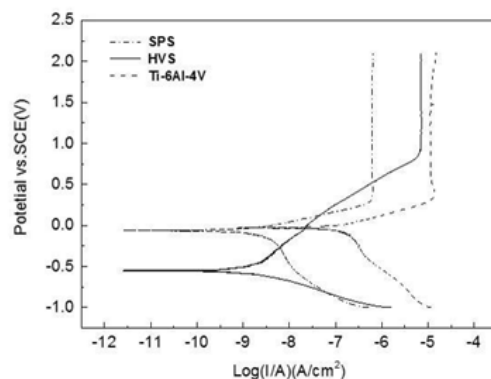


FIG.4. Potentiodynamic polarization curves of SPSed, HVSed and Ti-6Al-4V alloys in the Hank's solution at 37°C.

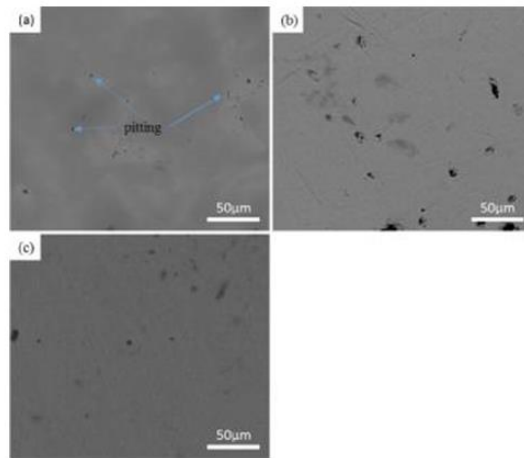
In order to investigate the protective oxide film, XPS was used and the results showed that the passive film of SPSed and HVSed alloy are mainly composed of  $\text{TiO}_2$ ,  $\text{Nb}_2\text{O}_5$  and  $\text{ZrO}_2$ , and the binding energies signal of Ti 2p at 458.2eV, Nb 3d at 206.5eV and Zr 3d at 183.2eV.

TABLE 1 Corrosion parameters of SPSed, HVSed and Ti-6Al-4V alloys in the Hank's solution at 37°C.

Alloy	$E_{\text{corr}}/\text{V}$	$I_{\text{corr}} (\text{mA}/\text{cm}^2)$	$I_{\text{pass}}(\text{mA}/\text{cm}^2)$
SPS	-0.062	0.026	0.618
HVS	-0.552	0.032	7.15
Ti-6Al-4V	-0.023	0.043	11.22

FIG. 5 showed SEM results of the samples after immersion in the Hank's solution for 72 hours. The three alloys exhibited different corrosion characteristics, and the SPSed alloy was less corrosive than the other two alloys. Besides, the results also showed that the corrosion of SPSed alloy firstly occurred in the rich-Nb area, mainly because the stress concentration lead to the corrosion [17]. In fact, many scholars have studied the effect of alloying elements on corrosion resistance of titanium alloys. Yu et al. [18] discussed the influence of Nb and Zr alloying element on electrochemical behavior of titanium alloy, and suggested that the addition of Nb and Zr improved the passivation properties compared with pure Ti. Pogers et al. [19] noted that Ti-6Al-7Nb owned superior corrosion resistance relative to the Ti6Al4V alloy. And Then, Liu et al. [20] reported that the  $\text{Nb}^{+5}$  cation can reduce the vacancy of anion and stabilize the tetragonal crystal structure of zirconium dioxide by

solid solution in zirconium dioxide and replacing  $Zr^{+4}$  cation, which helped hinder the migration of anions and improved the corrosion resistance of the alloy. Besides, the microstructure of the alloy also has a great influence on its corrosion resistance.



**FIG.5. SEM of the samples after immersion in the Hank’s solution for 72 hours (a) SPSed, (b) HVSeD and (c) Ti-6Al-4V.**

According to the Bode plot, we can see significant differences between the three materials. For the HVSeD alloy, in the low frequency region(10-1-102Hz), the phase angle is maintained at -75 degrees, and the slope of the f(frequency)-|Z|(impedance mode) curve is substantially-1, mainly due to the formation of the passivation film. Furthermore, in the high-frequency region (103-105Hz), the phase angle tends to 0 degrees and the slope of the frequency-impedance mode curve is substantially 0 because of the impedance of the electrode. For Ti6Al4V and SPSed alloys, the Bode plot reveals two time constants, mainly due to the formation of a double-layer passivation film composed of a looser outer passivation film and a dense inner passivation film. The other time constant corresponding to the low-frequency bands comes from the contribution of the electric double-layer capacitance of the inner dense passivation layer and the polarization resistance of the surface corrosion reaction.

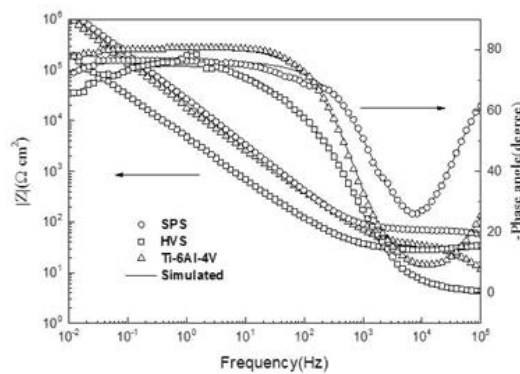


**FIG.6. Bode plots in the Hank’s solution at 37°C in which the symbols are the experimental results and the solid curves are the modeling.**

As shown in the  $f-|Z|$  curve of the SPSed alloy, we can see that in the range of 10-3-10-4Hz, which should be a linear platform, has a slope between -0.5 and -0.2, mainly due to the blocking effect of the passivation film, the electrolyte solution infiltrates inwardly through the void(s) of the loose layer of the passivation film, and the direction of the mass transfer process of the reaction particles is not parallel to the direction of the concentration gradient, which is called for tangential diffusion [21].

Based on the EIS data presented in **FIG. 6**, the  $R_s(Q1R1)$  model with only one time constant fits the interfacial behavior of the HVSed alloy which formed a single layer film on the surface as shown in **FIG.7 (a)**,  $R_s$  is the electrolyte impedance,  $R_1$  is the passivation film impedance, and  $Q_1$  is the constant phase angle element of the passivation film. Some researchers [22-24] also have shown that titanium and titanium alloy can form double layer passivation film during corrosion in simulated saliva, which contains a dense inner layer and a loose outer layer. Therefore, according to the above mentioned conclusion and the combination of the corrosion characteristics of Ti-6Al-4V and SPSed alloys in simulated body fluid, the equivalent circuit model  $R_s(Q1R1)(Q2R2)$  of double-layer passivation film was established as shown in **FIG.7 (b)**, of which the  $R_s$  is the solution resistance,  $Q_1$  and  $R_1$  is the phase angle element and resistance of surface passivation film,  $Q_2$  and  $R_2$  is the phase angle element and resistance of compact passivation film.  $N$  is related to the heterogeneity of current, roughness of sample and uneven distribution.

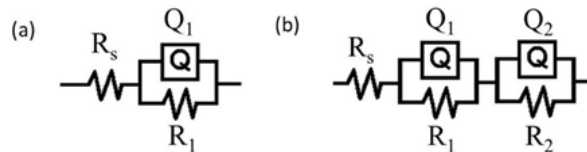


**FIG.7. Equivalent circuit fitted for three samples in the Hank’s solution at 37°C (a)for HVSed alloy and (b)for Ti-6Al-4V and SPSed alloys.**

Parameter analysis and data fitting of EIS curves were carried out using ZsimpWin software, the fitting results are shown in **TABLE 2**. It is obvious that the chi square fitting error of parameters in the equivalent circuit diagram is under 1%, additionally, the visible test values and fitting data coincided very well. Besides, both in the Ti-6Al-4V and SPSed alloys, the  $R_2$  value is larger than  $R_1$ , which means that the inner passivated film played a major role in the protection [25]. According to the value of  $R_2$ , the corrosion resistance of SPSed alloy is higher than that of HVSed. The results are consistent with that of the potentiodynamic polarization curve.

**TABLE 2. Electrical parameters of the equivalent circuits obtained by fitting the experimental results of EIS data together with the chi-square values.**

Materials	$R_s / (\Omega \text{ cm}^2)$	$R_1 / (M\Omega \text{ cm}^2)$	$Q_1 / (\mu\text{F}/\text{cm}^2)$	n1	$R_2 / (M\Omega \text{ cm}^2)$	$Q_2 / (\mu\text{F}/\text{cm}^2)$	n2	$\chi^2$
SPS	6.33	0.00002	0.496	0.981	1.72E+12	17.27	0.851	5.58'10-3
HVS	29.84	0.141	46.19	0.824	-	-	-	5.85'10-3
Ti-6Al-4V	5.136	0.00004	0.08	0.909	1.32E+12	11.74	0.898	9.47'10-4

It is worth pointing out that the corrosion resistance of the alloy is mainly affected by the composition, working environment, and microstructure. In the present study, the SPSed and HVSed alloys are able to form passivation film consisting of  $\text{Nb}_2\text{O}_5$ ,  $\text{ZrO}_2$  and  $\text{TiO}_2$ , which indicates that the corrosion resistance of these two types of alloys is relatively good. Yu et al [18] have shown that the addition of niobium and zirconium contributes to improving the corrosion resistance of titanium alloys, mainly because they can form strong covalent bonds among atoms by sharing unmatched d-level electrons. The difference in corrosion resistance between the two alloys is mainly caused by the microstructure, and studies [26,27] have reported that the corrosion first occurs at the  $\alpha/\beta$  interface, mainly due to the different rate of forming the passivation film on the surface of two phases. In addition, the galvanic interaction between the  $\alpha$  and  $\beta$  promotes the preferential dissolution of the two-phase interface.

## Conclusion

1. The Ti-40Nb-15Zr(at.%) alloy was prepared by traditional high vacuum sintering (HVS) technology and spark plasma sintering (SPS) using Zr, Nb, and Ti elemental powders, with the relative density of 89% and 98%, respectively. The SPSed alloy was characterized by rich-Nb phase which have little obvious effect on the corrosion performance in this study, and the HVSed alloy consisted of equiaxed  $\beta$  grains with a few fine intragranular  $\alpha$  needles.
2. Both the HVSed alloy and the SPSed alloy formed stable oxide passive films mainly consisted of  $\text{TiO}_2$ ,  $\text{Nb}_2\text{O}_5$  and  $\text{ZrO}_2$  on the surface of the alloy.
3. Furthermore, the EIS results demonstrated the existence of a duplex film consisting of an inner barrier layer and a porous outer layer on both Ti-6Al-4V and SPSed alloy.

## Acknowledgments

This work was financially supported by the National Natural Science Foundation of China (No.51404302).

## REFERENCES

1. Xie KY, Wang Y, Zhao Y, et al. Nanocrystalline  $\beta$ -Ti alloy with high hardness, low Young's modulus and excellent in vitro biocompatibility for biomedical applications. Mater Sci Eng C. 2013;33:3530-6.
2. Zhang J, Sun F, Hao Y, et al. Influence of equiatomic Zr/Nb substitution on superelastic behavior of Ti-Nb-Zr alloy. Mater Sci Eng A. 2013;563:78-85.

3. Nie L, Zhan Y, Hu T, et al.  $\beta$ -Type Zr–Nb–Ti biomedical materials with high plasticity and low modulus for hard tissue replacements. *J Mech Behav Biomed Mater.* 2014;29:1-6.
4. Nie L, Zhan Y, Liu H, et al. Novel  $\beta$ -type Zr–Mo–Ti alloys for biological hard tissue replacements. *Mater Design.* 2014;53:8-12.
5. Guo Q, Zhan Y, Mo H, et al. Aging response of the Ti–Nb system biomaterials with  $\beta$ -stabilizing elements. *Mater Design.* 2010;31:4842-6.
6. Guo S, Zhang J, Cheng et al. A metastable  $\beta$ -type Ti–Nb binary alloy with low modulus and high strength. *J Alloys Compd.* 2015;644:411-5.
7. Bai Y, Hao YL, Li SJ, et al. Corrosion behavior of biomedical Ti–24Nb–4Zr–8Sn alloy in different simulated body solutions. *Mater Sci Eng C.* 2013;33:2159-67.
8. Chaves JM, Florêncio O, Silva PS, et al. Anelastic relaxation associated to phase transformations and interstitial atoms in the Ti–35Nb–7Zr alloy. *J Alloys Comp.* 2014;616:420-5.
9. Sander B, Raabe D. Texture inhomogeneity in a Ti–Nb-based  $\beta$ -titanium alloy after warm rolling and recrystallization. *Mater Sci Eng A.* 2008;479:236-47.
10. Wang HL, Hao YL, He SY, et al. Elastically confined martensitic transformation at the nano-scale in a multifunctional titanium alloy. *Acta Mater.* 2017;135:330-9.
11. Gao R, Cao B, Hu Y, et al. Human infection with a novel avian-origin influenza A (H7N9) virus. *New England J Med.* 2013;368:1888-97.
12. Zhang J, Gan X, Tang H, et al. Enhancement of wear and corrosion resistance of low modulus  $\beta$ -type Zr-20Nb-xTi (x=0,3) dental alloys through thermal oxidation treatment. *Mater Sci Eng C.* 2017;76:260-8.
13. Jiang B, Wang Q, Wen D, et al. Effects of Nb and Zr on structural stabilities of Ti-Mo-Sn-based alloys with low modulus. *Mater Sci Eng A.* 2017;687:1-7.
14. Correa DRN, Vicente FB, Donato TG, et al. *Mater Sci Eng C* 2014;34:354.
15. Cvijović-Alagić I, Cvijović Z, Mitrović S, et al. Wear and corrosion behaviour of Ti–13Nb–13Zr and Ti–6Al–4V alloys in simulated physiological solution. *Corros Sci.* 2011;53:796-808.
16. Marino CE, de Oliveira EM, Rocha-Filho RC, et al. On the stability of thin-anodic-oxide films of titanium in acid phosphoric media. *Corros Sci.* 2001;43:1465-76.
17. Bin ZL, Hong Y, Yuan YH, et al. *J Central South Uni.* 2017;24:1934.
18. Steven YY, Scully JR, Vitus CM. Influence of niobium and zirconium alloying additions on the anodic dissolution behavior of activated titanium in HCl solutions. *J Electrochem Soci.* 2001;148:B68-78.
19. Rogers SD, Howie DW, Graves SE, et al. In vitro human monocyte response to wear particles of titanium alloy containing vanadium or niobium. *J Bone Joint Surgery. British volume.* 1997;79:311-5.
20. Yao MY, Zhou BX, Li Q, et al. A superior corrosion behavior of Zircaloy-4 in lithiated water at 360 C/18.6 MPa by  $\beta$ -quenching. *J Nucl Mater.* 2008;374:197-203.
21. Zhang JQ, Cao CN; *Corro. Protect,* 3, 99 (1998).

22. Milošev I, Metikoš-Huković M, Strehblow HH. Passive film on orthopaedic TiAlV alloy formed in physiological solution investigated by X-ray photoelectron spectroscopy. *Biomater.* 2000;21:2103-13.
23. Fekry AM, El-Sherif RM. Electrochemical corrosion behavior of magnesium and titanium alloys in simulated body fluid. *Electrochimica Acta.* 2009;54:7280-5.
24. Tamilselvi S, Raman V, Rajendran N. Corrosion behaviour of Ti-6Al-7Nb and Ti-6Al-4V ELI alloys in the simulated body fluid solution by electrochemical impedance spectroscopy. *Electrochimica Acta.* 2006;52:839-46.
25. Bai YJ, Wang YB, Cheng Y, et al. Comparative study on the corrosion behavior of Ti-Nb and TMA alloys for dental application in various artificial solutions. *Mater Sci Eng C.* 2011;31:702-11.
26. He X, Noel JJ, Shoesmith DW. Effects of iron content on microstructure and crevice corrosion of grade-2 titanium. *Corros.* 2004;60:378-86.
27. Xu YF, Xiao YF, Yi DQ, et al. Corrosion behavior of Ti-Nb-Ta-Zr-Fe alloy for biomedical applications in Ringer's solution. *Transactions of Nonferrous Metals Society of China.* 2015;25:2556-63.